

Autonomous Robotic Bone Micro-Milling System with Automatic Calibration and 3D Surface Fitting

Enduo Zhao, Xiaofeng Lin, Yifan Wang, and Kanako Harada

Abstract—Automating bone micro-milling using a robotic system presents challenges due to the uncertainties in both the external and internal features of bone tissue. For example, during a mouse cranial window creation, a circular path with a radius of 2 to 4 mm needs to be milled on the mouse skull using a microdrill. The uneven surface and non-uniform thickness of the mouse skull make it difficult to fully automate this process, requiring the system to possess advanced perceptual and adaptive capabilities. In this study, we propose an automatic calibration and 3D surface fitting method and integrate it into an autonomous robotic bone micro-milling system, enabling it to quickly, in real-time, and accurately perceive and adapt to the uneven surface and non-uniform thickness of the target without human assistance. Validation experiments on euthanized mice demonstrate that the improved system achieves a success rate of 85.7 % and an average milling time of 2.1 minutes, showing not only significant performance improvements over the previous system but also exceptional accuracy, speed, and stability compared to human operators.

I. INTRODUCTION

Bone micro-milling is an essential biological operation that involves using specialized milling tools to precisely remove or shape bone tissue at a microscale level [1]. This demands a high level of skill from the human operator due to the tiny scale and the need for high accuracy and safety. Automating this process with a robotic system could, in principle, make it more accurate and reproducible than by a human operator. However, this presents challenges for the perceptual and adaptive capabilities of the robotic system. The system needs to first accurately perceive the uncertainties in the characteristics of the bone tissue, including external features such as initial pose and surface flatness, as well as internal features like thickness and heterogeneity [2], and then generate milling trajectories that can adapt to these uncertainties.

For instance, in scientific experiments involving the transplantation of human organoids into mice and monitoring their growth [3], an important preparatory step is creating a circular cranial window with a radius of 2 to 4 mm on the mouse skull, whose thickness varies unevenly from 0.27 to 0.51 mm, depending on the strain, sex, and age of the mouse. To avoid damaging the fragile membrane beneath, skilled human operators typically use a handheld

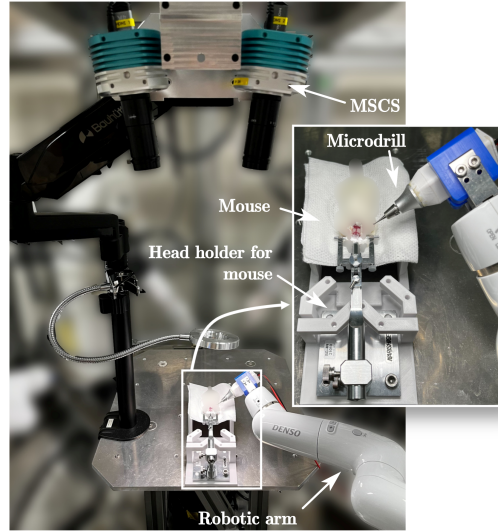


Fig. 1. The hardware setup of the autonomous robotic bone micro-milling system, including a robotic arm holding a microdrill, a head holder for mouse to be milled, and a Microscopic Stereo Camera System (MSCS).

microdrill to mill the skull to an extremely thin thickness along the trajectory under the observation of a high magnification microscope, and then remove the central bone flap with tweezers. Therefore, when attempting to automate this process, the system must control the movement of the drill bit to ensure that all positions along the circular trajectory on the skull reach the same expected remaining thickness simultaneously. However, the surface of the mouse skull is uneven, and its thickness varies, making this process very complex. Additionally, these features dynamically change due to the potential skull deformation caused by contact with the drill bit during the milling process. Thus, the system must not only possess autonomous and accurate perception capabilities for the uneven surface and non-uniform thickness of the mouse skull, but also be able to rapidly and in real time adapt to their dynamic changes during the milling process.

A. Related Works

Many studies developed robotic systems for automated cranial window creation and attempted to pre-measure the skull's surface information and thickness for milling trajectory planning. Pak et al. [4] measures surface position and thickness by drilling at pre-set test points while detecting changes in conductivity between the drill tip and the skull. Ghanbari et al. [5] used micro-CT, while Navabi et al. [6] combined optical coherence tomography (OCT) and machine

*This work was supported by JST Moonshot R&D JPMJMS2033.

Enduo Zhao and Yifan Wang are with the Department of Mechanical Engineering, Graduate School of Engineering, The University of Tokyo, Tokyo, Japan. Xiaofeng Lin and Kanako Harada is with the Center for Disease Biology and Integrative Medicine, Graduate School of Medicine, The University of Tokyo, Tokyo, Japan. Emails: {endowzhao1996, wang-yifan971125, lin-xiaofeng, kanakoharada}@g.ecc.u-tokyo.ac.jp.

learning, to obtain the skull anatomy. Jeong et al. [7] utilized an ultrashort pulsed Ti-sapphire oscillator to generate and detect second harmonic light for the metrology of the skull. Nonetheless, the above methods lack a feedback mechanism, making it impossible to make real-time adaptation to the dynamic changes in the skull’s characteristics.

In the prior research by the present authors [8], an autonomous robotic bone micro-milling system was developed based solely on real-time 2D image feedback. The system utilized a convolutional neural network (CNN) to recognize the milling completion level of trajectory points from the input RGB images during the milling process, providing real-time feedback for the adaptive updating of the milling trajectory. The performance of the system was evaluated by 20 eggshell milling experiments, achieving a success ratio of 80% and average milling time of 16.8 minutes. However, due to the lack of direct measurement on the surface, the system could only adapt to the uneven surface relying on real-time feedback after milling starts, which led to a prolonged milling time and several cases of milling failure. Moreover, before autonomous milling begins, the drill bit must be manually teleoperated to a starting position where the distance between the bit and the surface is appropriate, requiring assistance from a skilled human operator.

B. Statement of contributions

In this study, we propose a method of automatic calibration and 3D surface fitting based on the the Microscopic Stereo Camera System (MSCS), allowing rapid surface measurement and initial trajectory generation without human assistance. By integrating it with the system in the prior research by the present authors, we have developed the world’s first autonomous robotic bone micro-milling system capable of perceiving the uneven surface through pre-measurement and adapting to the non-uniform thickness and dynamic changes through real-time feedback, whose performance and efficiency has been validated through cranial window creation experiments on euthanized mice.

II. HARDWARE SETUP AND SYSTEM OVERVIEW

The hardware setup of the system is shown in Fig. 1, utilizing a single-arm setup from the Multiarm Robotic Platform for scientific exploration [9]. The setup includes a robotic arm (CVR038, Densowave, Japan), a linear actuator and a circular rail actuator, which can be regarded as an 8-degree-of-freedom serial manipulator with joint values $q \in \mathbb{R}^8$. The robotic arm is equipped with a micro drill (MD1200, Braintree Scientific, USA) designed to mill the mouse skull secured in a head holder (SG-4N, NARISHIGE, Japan). To accommodate the confined workspace of the robotic system room, a modified MSCS setup was developed based on the original desktop MSCS setup (developed by the present authors [10]), consisting of two cameras (STC-HD853HDMI, Omron-Sentech, Japan) fitted with low-distortion macro lenses (VS-LDA75, VS Technology, Japan). The MSCS provides a reconstruction space of approximately $20 \times 30 \times 10$ mm with a depth resolution of 0.10 ± 0.02 mm

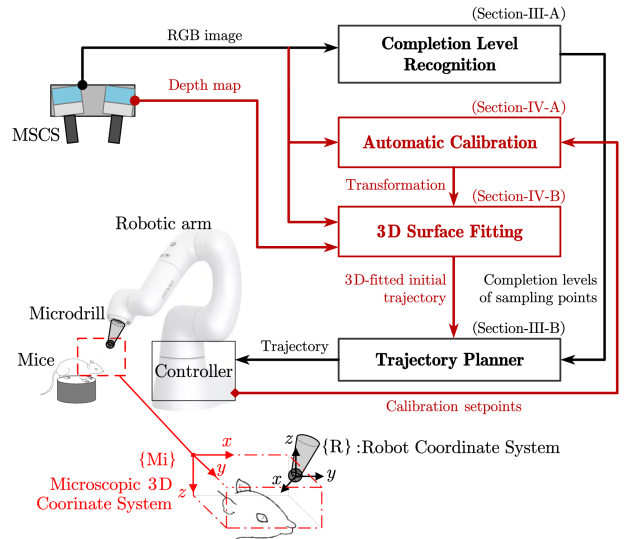


Fig. 2. Overview of the autonomous robotic bone micro-milling system integrated with the proposed method. The parts in black are modified from the original system, while the parts in red are newly added in this work. Additionally, the robot coordinate system $\{R\}$ and the microscopic 3D coordinate system $\{Mi\}$ are illustrated at the bottom of the figure.

that is sufficient for reconstructing the mouse skull [10], and a working distance of around 500 mm that meets the requirements for robotic movement [9].

The overview of the system integrated with the proposed method is shown in Fig. 2. The Completion Level Recognition and the Trajectory Planner, which are modified to serve as the foundation of this work based on the previous system [8], will be introduced in Section III. The Automatic Calibration and the 3D Surface Fitting, which are the main contributions of this work, will be introduced in Section IV.

III. MATERIAL AND METHODS

In this section, the Completion Level Recognition (Section III-A) and the Trajectory Planner (Section III-B) are introduced, which are modified from the autonomous robotic bone micro-milling system in the prior research by the present authors [8]. In the detailed description, which parts remain unchanged and which have been improved will be highlighted.

A. Completion Level Recognition

The Completion Level Recognition module is consistent with the previous system. Based on the RGB image input from either camera, this module uses a CNN to detect the drilling area and recognize the completion level for each pixel, generating a completion level heatmap. Through post-processing, a progress bar is created to reflect the milling progress along the trajectory. An example of the input image (with detected drilling area), the corresponding completion level heatmap and the progress bar is shown in Fig. 3-(a). Then, by setting n discrete points evenly along the circle on the progress bar, an n -dimensional vector c can be obtained, in which element denotes the penetration percentage at the

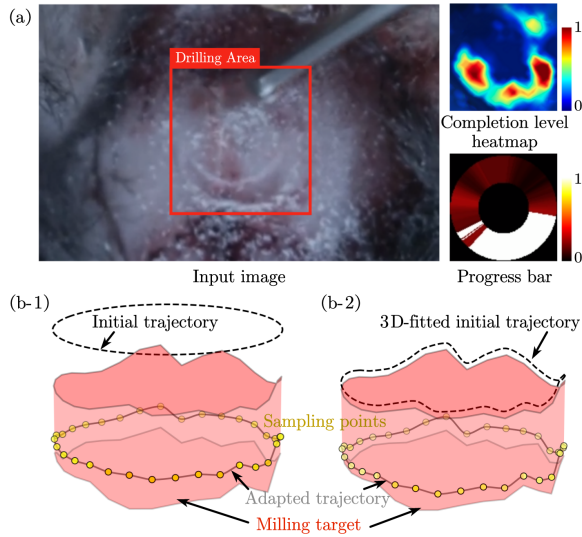


Fig. 3. Schemas of (a) an example of the input and output of Completion Level Recognition; (b-1) the Trajectory Planner in the previous system, and (b-2) the Trajectory Planner in this study.

i -th sampling point along the real-time-updated trajectory, defined by

$$\mathbb{R} \ni c_i \triangleq c_i(t) \in [0, 1], \quad (1)$$

where $i = 1, 2, \dots, n$. Note that $c_i = 0$ means untouched and $c_i = 1$ means completely penetrated. c is output to the Trajectory Planner for real-time trajectory updates.

B. Trajectory Planner

As the foundation of this study, we will first describe the Trajectory Planner of the previous system and then propose improvements. Considering that the robot must obtain a continuous trajectory for smooth performance using our inverse kinematics calculation [9], the number of trajectory points N needs to be sufficiently large, but the resolution limitation of RGB images makes it impossible to make effective real-time perception of all trajectory points by the Completion Level Recognition (Section III-A), resulting in the length of its output vector c to be $n \ll N$. Therefore, we first initialize and real-time update the trajectory at n sampling points, and then connect these points through interpolation to obtain a sufficiently continuous trajectory.

In formal terms, by discretizing the milling trajectory into n equal intervals, n sampling points $\mathbf{p}_i \triangleq [x_i \ y_i \ z_i]^T \in \mathbb{R}^3, i = 1, \dots, n \in \mathbb{N}$ can be obtained, defined with respect to the robot coordinate system $\{\mathbf{R}\}$ (see Fig. 2). Considering that the trajectory is circular when projected onto the x - y plane, x_i and y_i remain constant while z_i is initialized and real-time updated based on the two inputs.

The first input is for initialization, named the initial trajectory $\mathbf{p}_{ini,i}$, an n -dimensional vector where each element stands for the coordinate of the i -th sampling point along the initial trajectory with respect to $\{\mathbf{R}\}$, defined by

$$\mathbf{p}_{ini,i} \triangleq [x_{ini,i} \ y_{ini,i} \ z_{ini,i}]^T \in \mathbb{R}^3, \quad (2)$$

where $i = 1, 2, \dots, n$. As mentioned above, the x and y coordinates of trajectory keep unchanged during milling process, implying $x_i \equiv x_{ini,i}$ and $y_i \equiv y_{ini,i}$. In the previous system, due to the lack of direct measurement on surface, the z -coordinate of each sampling point on the initial trajectory was set as $z_{ini,i} = 0 \ \forall i = 1, \dots, n \in \mathbb{N}$ (see Fig. 3-(b-1)), thus, z_i is initialized by

$$z_i(t=0) = 0. \quad (3)$$

The second input is for real-time update, named the completion levels of sampling points c , output from the Completion Level Recognition and defined by (1). The core of the updating strategy is to proportionally reduce the vertical velocity $v_{z,i} \triangleq v_{z,i}(c_i) \in \mathbb{R}$ of the i -th sampling point based on its completion level c_i . The velocity is modulated as follows

$$v_{z,i}(c_i) = (1 - c_i)v_z. \quad (4)$$

where v_z is a nominal velocity and $v_z < 0$. (4) implies that when the completion level of the sampling point is $c_i = 0$, the point remains untouched, and the vertical velocity is $v_{z,i}(0) = v_z$, meaning the robot moves downward at the nominal velocity. In contrast, when $c_i = 1$, the point is completely penetrated, resulting in a downward velocity of $v_{z,i}(1) = 0$, indicating that the robot ceases further descending at that point. For intermediate completion levels, the system transitions smoothly, adjusting the velocity proportionally to the completion level.

Considering the integration of (4) with a sampling time T , the position can be updated by

$$z_i(t+T) = z_i(t) + v_{z,i}(c_i)T. \quad (5)$$

So far, the z -axis coordinates for all of the n discrete sampling points have been initialized by (3) and updated by (5). To obtain a continuous trajectory and avoid potential overshooting problem, additional k points are inserted between any two adjacent points \mathbf{p}_i and \mathbf{p}_{i+1} by constrained spline interpolation [11], expanding the total number of trajectory points to $n(k+1)$. By selecting the value of k such that $n(k+1) > N$, the high-precision encoders used in the robotic system can be matched. Fig. 3-(b-1) shows the trajectory adapting to the milling target, initialized and updated by the Trajectory Planner in the previous system.

In this study, the Trajectory Planner is improved by the surface information obtained through the introduction of the MSCS and the method proposed in Section IV so that the $z_{ini,i}$ in (2) becomes non-zero and adapts to the uneven surface, as shown in Fig. 3-(b-2). To distinguish, we refer to the initial trajectory of the improved system as the 3D-fitted initial trajectory, which is output from 3D Surface Fitting (Section IV-B). As a result, the z -axis coordinate z_i of the i -th sampling point on the trajectory can be initialized by $z_i(t=0) = z_{ini,i}$ and updated by (5).

Additionally, we hypothesize that if all n sampling points are completely penetrated, the entire trajectory will be sufficiently milled using the constrained spline interpolation

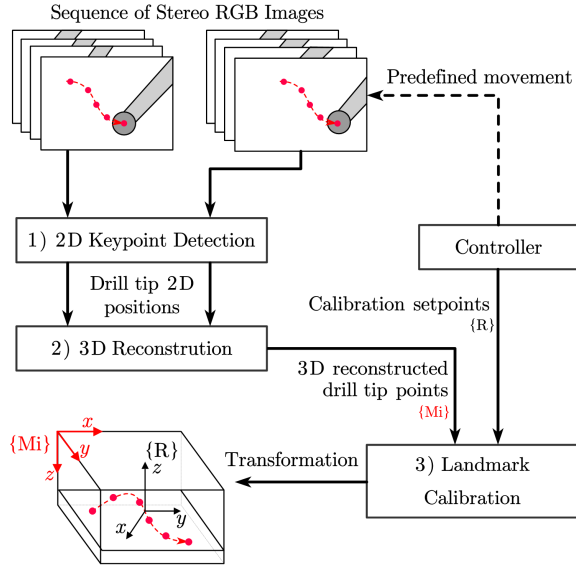


Fig. 4. The workflow of the Automatic Calibration.

method. Therefore, when $c_i = 1 \quad \forall i = 1, \dots, n \in \mathbb{N}$, a stop signal will be triggered and sent to the controller to automatically halt the robot's movement and the drill's rotation, marking the completion of the milling process.

IV. PROPOSED METHOD

The proposed method aims to provide the Trajectory Planner with the 3D-fitted initial trajectory p_{ini} for initialization, based on RGB images and depth maps. In this section, the Automatic Calibration (Section IV-A), which determines the transformation from the microscopic 3D coordinate system $\{Mi\}$ to the robot coordinate system $\{R\}$ (see Fig. 2), and the 3D Surface Fitting (Section IV-B), which samples trajectory points on the surface of bone tissue at appropriate locations and transforms them to $\{R\}$, are described in detail.

A. Automatic Calibration

With the introduction of MSCS, the point clouds of the target surface can be reconstructed with respect to $\{Mi\}$ using the model in the prior research by the present authors [10]. Since the milling trajectory must be planned with respect to $\{R\}$, it is essential to determine the transformation matrix from $\{Mi\}$ to $\{R\}$ through calibration. However, due to the limited workspace at the microscale and insufficient features on the microdrill, traditional calibration methods become impractical, such as attaching Aruco markers [12] or checkerboard patterns [13] to the end-effector, or identifying landmarks based on the end-effector's features [14].

By exploiting the fact that in our system, the drill tip can be controlled to reach any desired points with respect to $\{R\}$ through inverse kinematics as landmarks, if we can obtain the coordinates of these landmarks with respect to $\{Mi\}$, the calibration problem between $\{Mi\}$ and $\{R\}$ can be solved. Therefore, in this section, we propose an Automatic Calibration method, achieving automatic, rapid, and real-time calibration without human assistance, as shown

in Fig. 4. The method consists of 2D Keypoint Detection to detect the drill tip 2D positions based on the input RGB images, 3D Reconstruction to obtain 3D reconstructed drill tip points, and Landmark Calibration to solve the calibration problem between $\{Mi\}$ and $\{R\}$ by combining the calibration setpoints, with respect to $\{R\}$, with the corresponding 3D reconstructed drill tip points, with respect to $\{Mi\}$.

1) *2D Keypoint Detection*: To reconstruct the 3D points of the drill bit, its 2D projection coordinates in both the left and right images are required. This is primarily due to its small size, as directly accessing the reconstructed point clouds would lead to a suboptimal result. Therefore, a keypoint-detection CNN is utilized to obtain the drill tip 2D positions in both images. The CNN used is a minor adjustment of U-Net [15], where the adjustments include changing the input ground truths from segmentation masks to confidence maps of drill tip localization. By this, the drill tip 2D positions $p_l \triangleq [x_l \ y_l]^T \in \mathbb{R}^2$ (pixel) in the left image and $p_r \triangleq [x_r \ y_r]^T \in \mathbb{R}^2$ (pixel) in the right image can be obtained by locating the local maximum from the predicted confidence map.

2) *3D Reconstruction*: Based on the two detected drill tip 2D positions, the 3D position of the drill tip $p_d^{\{Mi\}} \in \mathbb{R}^3$ with respect to $\{Mi\}$ can be reconstructed by:

$$p_d^{\{Mi\}} = M_d \begin{bmatrix} p_l \\ p_r \end{bmatrix} + b_d, \quad (6)$$

where $M_d \in \mathbb{R}^{3 \times 4}$ is the coefficient matrix and $b_d \in \mathbb{R}^{3 \times 1}$ is the bias, whose values can be calculated using the streamlined linear model of disparity-depth mapping function (detailed in [10]):

$$M_d = \begin{bmatrix} P_{\rho x} & 0 & 0 & 0 \\ P_{\rho y} & 0 & 0 & 0 \\ \frac{1}{h_\rho} & 0 & -\frac{1}{h_\rho} & 0 \end{bmatrix}, \quad b_d = \begin{bmatrix} -c_x P_{\rho x} \\ -c_y P_{\rho y} \\ d_e \end{bmatrix}, \quad (7)$$

where c_x, c_y (pixel) are the camera's principal point image coordinates, $P_{\rho x}, P_{\rho y}$ (pixel/mm) respectively indicate the object's pixel sizes in the x and y directions, d_e (mm) is the effective working distance of the stereo microscope setup, and h_ρ (pixel/mm) denotes the depth response to unit disparity in reality. All parameters in (7) have been measured and calculated in [10]. By substituting (7) into (6), the 3D position of the reconstructed drill tip can be calculated.

3) *Landmark Calibration*: Landmark Calibration aims to determine the rigid transformation from $\{Mi\}$ to $\{R\}$ based on the corresponding landmarks. The transformation is defined as

$$T_{\{Mi\} \rightarrow \{R\}} \triangleq \begin{bmatrix} \mathbf{R} & \mathbf{t} \\ 0 & 1 \end{bmatrix}, \quad (8)$$

where $\mathbf{R} \in \mathbb{R}^{3 \times 3}$ is the rotation matrix and $\mathbf{t} \in \mathbb{R}^{3 \times 1}$ is the translation vector.

To obtain the corresponding landmarks, the controller sends a sequence of calibration setpoints to move the drill tip, represented as $p_i^{\{R\}} \in \mathbb{R}^3, i = 1, \dots, k \in \mathbb{N}$ with respect

to $\{R\}$. For each setpoint, two images are captured from left and right cameras in MSCS and its 3D position with respect to $\{Mi\}$ can be reconstructed by (6). Thus, a sequence of 3D reconstructed drill tip points with respect to $\{Mi\}$ can be obtained, represented as $\mathbf{p}_i^{\{Mi\}} \in \mathbb{R}^3, i = 1, \dots, k \in \mathbb{N}$. Note that at least $k \geq 3$ non-collinear points are required to uniquely determine the transformation.

In order to compute \mathbf{R} and \mathbf{t} in (8), firstly the centroids of $\mathbf{p}_i^{\{Mi\}}$ and $\mathbf{p}_i^{\{R\}}$ are calculated by

$$\mathbf{c}^{\{Mi\}} = \frac{1}{k} \sum_{i=1}^k \mathbf{p}_i^{\{Mi\}}, \quad \mathbf{c}^{\{R\}} = \frac{1}{k} \sum_{i=1}^k \mathbf{p}_i^{\{R\}}. \quad (9)$$

Then centralize $\mathbf{p}_i^{\{Mi\}}$ and $\mathbf{p}_i^{\{R\}}$ by subtracting (9):

$$\mathbf{q}_i^{\{Mi\}} = \mathbf{p}_i^{\{Mi\}} - \mathbf{c}^{\{Mi\}}, \quad \mathbf{q}_i^{\{R\}} = \mathbf{p}_i^{\{R\}} - \mathbf{c}^{\{R\}}. \quad (10)$$

Next, calculate the covariance matrix \mathbf{H} using the result in (10) and perform Singular Value Decomposition (SVD):

$$\mathbf{H} = \sum_{i=1}^k \mathbf{q}_i^{\{R\}} \left(\mathbf{q}_i^{\{Mi\}} \right)^T = \mathbf{U} \mathbf{\Sigma} \mathbf{V}. \quad (11)$$

Thus, the rotation matrix \mathbf{R} can be computed from the SVD results in (11):

$$\mathbf{R} = \mathbf{V} \mathbf{U}^T. \quad (12)$$

Note that in (12) if $\det(\mathbf{R}) < 0$, the last column of \mathbf{V} needs to be negated to ensure the orthogonality of the rotation matrix. And the translation vector \mathbf{t} can be computed by subtracting (9) and (12):

$$\mathbf{t} = \mathbf{c}^{\{Mi\}} - \mathbf{R} \mathbf{c}^{\{R\}}. \quad (13)$$

Finally, by substituting (12) and (13) into (8), the transformation matrix $\mathbf{T}_{\{Mi\} \rightarrow \{R\}}$ can be obtained.

B. 3D Surface Fitting

In this section, the goal is to generate an initial trajectory that is 3D fitted to the surface of the target, with its center point determined through the Trajectory Center Localization and trajectory points distributed on the circular path being sampled and biased through 3D-fitted Initial Trajectory Generation.

1) *Trajectory Center Localization:* In the actual experiment of mice cranial window creation, the center of the circular milling trajectory is always located between two specific anatomical points on the skull: bregma and lambda, as illustrated in Fig. 5. Inspired by the method in [16], which uses a CNN to automatically detect bregma and lambda, we applied a U-Net-based CNN with the same architecture as the one in Section IV-A.1 for the detection of these two points.

In practice, the ratio l of the distance between the trajectory center and bregma to the distance between bregma and lambda is determined based on the radius of the milling trajectory r and the size of the mouse. Therefore, the 2D position of the trajectory center in the input image can be

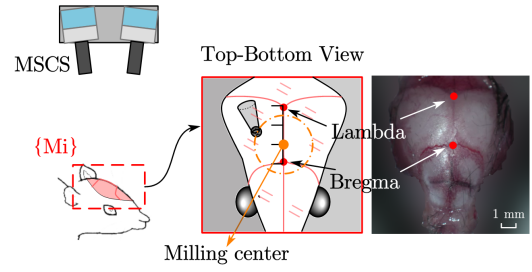


Fig. 5. Schematic of bregma and lambda, which is expected to be detected through the CNN. The milling center can be calculated by linearly weighting the two points.

obtained by proportionally weighting the detected positions of bregma and lambda. Then, due to the high-quality reconstruction of the skull surface, the 3D localization of the trajectory center $\mathbf{p}_c^{\{Mi\}} \triangleq [x_c \ y_c \ z_c]^T \in \mathbb{R}^3$ with respect to $\{Mi\}$ can be performed by accessing its 2D position in the RGB image from either camera and the reconstructed point cloud of the target surface (detailed in [10]).

2) *3D-fitted Initial Trajectory Generation:* Considering the expected trajectory is circular when projected onto the x - y plane, by combining the obtained trajectory center $\mathbf{p}_c^{\{Mi\}}$ and the radius of the milling trajectory r , the x and y coordinates of n sampling points along the trajectory $\mathbf{p}_{fit,i}^{\{Mi\}} \triangleq [x_{fit,i} \ y_{fit,i} \ z_{fit,i}]^T \in \mathbb{R}^3, i = 1, \dots, n \in \mathbb{N}$, with respect to $\{Mi\}$, can be calculated by:

$$\begin{aligned} x_{fit,i} &= r \cos \theta_i + x_c \\ y_{fit,i} &= r \sin \theta_i + y_c, \end{aligned} \quad (14)$$

where $\theta_i = 2\pi i/n, i = 1, \dots, n \in \mathbb{N}$. Then $z_{fit,i}$ can be obtained by combining $x_{fit,i}, y_{fit,i}$ and the reconstructed point cloud of the target surface.

In order to avoid contact with the surface even before milling, an offset should be set for all sampling points along their normal directions, considering the radius of the drill tip r_d and the potential error of Automatic Calibration. The normal vectors of all sampling points $\mathbf{n}_i \in \mathbb{R}^3, i = 1, \dots, n \in \mathbb{N}$ can also be obtained by the reconstructed point cloud of the target surface. As a result, by substituting the result of (14), the 3D-fitted initial trajectory $\mathbf{p}_{ini,i}^{\{Mi\}}$ with respect to $\{Mi\}$ can be obtained, whose each element can be calculated by

$$\mathbf{p}_{ini,i}^{\{Mi\}} = \mathbf{p}_{fit,i}^{\{Mi\}} + (r_d + \Delta d) \cdot \mathbf{n}_i. \quad (15)$$

where Δd is a manually set offset for safety concerns.

Lastly, utilizing the transformation matrix output from Automatic Calibration by (8), we can acquire the n -dimensional vector of transformed 3D-fitted initial trajectory \mathbf{p}_{ini} with respect to $\{R\}$, whose each element is defined by (2) and can be calculated by

$$\begin{bmatrix} \mathbf{p}_{ini,i} \\ 1 \end{bmatrix} = \mathbf{T}_{\{Mi\} \rightarrow \{R\}} \cdot \begin{bmatrix} \mathbf{p}_{ini,i}^{\{Mi\}} \\ 1 \end{bmatrix}. \quad (16)$$

The result of (16) is output to the Trajectory Planner for the initialization of the milling trajectory by (5).

V. EXPERIMENTS

In this section, experiments are conducted to validate the feasibility of the Automatic Calibration, the 3D Surface Fitting and the entire autonomous robotic bone micro-milling system.

A. System configuration

The software implementation of the experiments was carried out on an Ubuntu 20.04. The robotic arm was controlled following the approach in [9]. ROS (Robot Operating System) Noetic Ninjemys was utilized for interprocess communication, while simulations were conducted using CoppeliaSim (Coppelia Robotics, Switzerland). Communication with the robot was managed via the SmartArmStack¹. Dual quaternion algebra and robot kinematics were implemented using DQ Robotics [17] in Python 3.

B. Parameter selection

To implement the proposed method for validations and experiments, the parameters mentioned in Section III are selected to be the same as those in the prior research by the present authors [8]: the number of trajectory sampling points $n = 32$, the required number of trajectory points for smooth performance $N = 3000$, the number of inserted points for interpolation $k = 160$, the nominal velocity $v_z = -0.05$ mm/s, the sampling time $T = 0.004$ s. The parameters mentioned in Section IV are selected based on actual measurements, safety considerations, and ease of calculation: the ratio of the distance between the trajectory center and bregma to the distance between bregma and lambda $l = 1/3$, the radius of the milling trajectory $r = 2$ mm, the radius of the drill tip $r_d = 0.5$ mm, the manually set offset $\Delta d = 0.5$ mm, the number of calibration setpoints $k = 5$ and their coordinates $\mathbf{p}_1^{\{R\}} = [0 \ -20 \ 0]^T$, $\mathbf{p}_2^{\{R\}} = [10 \ -20 \ 0]^T$, $\mathbf{p}_3^{\{R\}} = [5 \ -10 \ 0]^T$, $\mathbf{p}_4^{\{R\}} = [10 \ 0 \ 0]^T$, $\mathbf{p}_5^{\{R\}} = [0 \ 0 \ 0]^T$ mm. Additionally, the resolution of the images captured by the MSCS is set to be 540×960 to meet the requirement of Automatic Calibration, 3D Surface Fitting, and Completion Level Recognition.

C. Experiment 1: Validation of Automatic Calibration

As described in Section IV-A, the accuracy of Automatic Calibration is affected by the accuracy of 2D Keypoint Detection, 3D Reconstruction, and Landmark Calibration. Considering the 3D Reconstruction depends on the MSCS, whose accuracy has been evaluated in the prior research by the present authors [10], in Experiment 1, we focus on the evaluation of 2D Keypoint Detection and Landmark Calibration.

1) *Training of 2D Keypoint Detection model:* To prepare learning data, a total of 3,294 images satisfying the requirement that the drill tip is within the field of view were captured from videos of teleoperated robotic cranial window creation experiments conducted on 10 euthanized mice. The mice were sacrificed for another research and reused in this

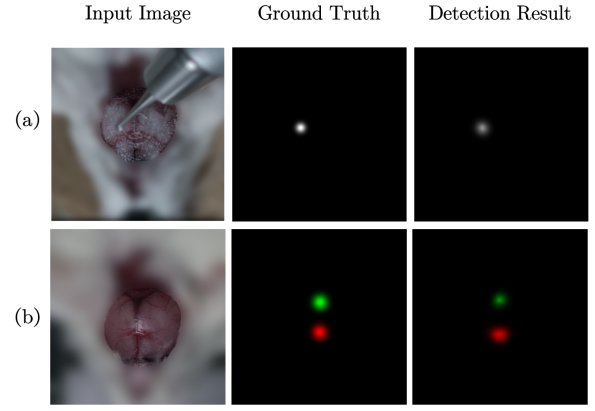


Fig. 6. Examples of the input image, ground truth, and detection result for the keypoint detection CNNs on (a) the drill tip and (b) bregma and lambda. The ground truth and detection result images are confidence maps, where pixels with brighter colors indicate a higher probability of being keypoint locations (while: drill tip, red: bregma, green: lambda).

study, so no additional ethical approval was required. For each image, a confidence map is generated by applying a 2D Gaussian distribution to the manually annotated drill tip 2D position, which represents the probability of the drill tip's existence and serves as the ground truth (an example is shown in Fig. 6-(a)). Data augmentation techniques, including blur and noise augmentation, color adjustment, geometric transformation, and resolution alteration, resulted in a total of 16,394 images and corresponding ground truths, with 14,754 images used for training, 820 for validation, and 820 for testing.

The models were trained in a total of 30 epochs using the Adam optimizer, with the training loss computed based on the Mean Square Error (MSE) criterion. The training rate was initialized as 1×10^{-3} , followed by a reduction to 1×10^{-4} in epochs 11 to 20, and further decreased to 1×10^{-5} for epochs 21 to 30. Moreover, a batch size of 4 was employed during the training phase. All models were implemented using PyTorch 1.8.0 with CUDA 11.1, based on Python 3.8, and executed on an Ubuntu 20.04 system equipped with an NVIDIA Quadro P6000 graphics card.

2) *Joint evaluation metrics:* Firstly, we send the robot $m = 20$ validation setpoints $\mathbf{p}_{val,i}^{\{R\}} \in \mathbb{R}^3, i = 1, \dots, m$ for the drill tip to reach these points. MSCS captures m images each from left and right camera, outputting m drill tip 2D positions each $\mathbf{p}_{l,i}, \mathbf{p}_{r,i} \in \mathbb{R}^2, i = 1, \dots, m$ via 2D Keypoint Detection (see Section IV-A.1). Then we manually annotate the left and right images, obtaining m ground truths each $\mathbf{p}_{l,i}^{(gt)}, \mathbf{p}_{r,i}^{(gt)} \in \mathbb{R}^2, i = 1, \dots, m$. Through 3D Reconstruction (see Section IV-A.2), m 3D reconstructed drill tip points with respect to $\{Mi\}$ can be obtained. Then, by transforming these points back to $\{R\}$ using the transformation calculated from Landmark Calibration (see Section IV-A.3), we can obtain $\mathbf{p}_{trans,i}^{\{R\}} \in \mathbb{R}^3, i = 1, \dots, m$. The accuracies of 2D Keypoint Detection and Landmark Calibration are respectively evaluated by the Root Mean Square Error (RMSE) between $\mathbf{p}_{l,i}, \mathbf{p}_{r,i}$ and $\mathbf{p}_{l,i}^{(gt)}, \mathbf{p}_{r,i}^{(gt)}$,

¹<https://github.com/SmartArmStack>

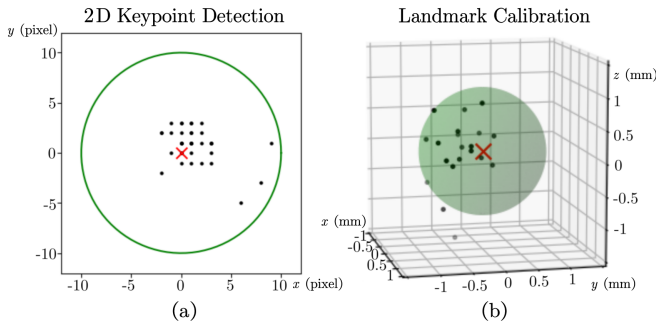


Fig. 7. Evaluation results of (a) 2D Keypoint Detection and (b) Landmark Calibration on 20 validation setpoints. The black dots, red cross and green circle or sphere respectively represent (a) the centralized $\mathbf{p}_{l,i}$, $\mathbf{p}_{r,i}$, the centralized $\mathbf{p}_{l,i}^{(gt)}$, $\mathbf{p}_{r,i}^{(gt)}$, the accuracy requirement of 10 pixels; (b) the centralized $\mathbf{p}_{trans,i}^{\{R\}}$, the centralized $\mathbf{p}_{val,i}^{\{R\}}$, and the accuracy requirement of 1 mm.

and between $\mathbf{p}_{trans,i}^{\{R\}}$ and $\mathbf{p}_{val,i}^{\{R\}}$.

Given the image resolution (of 540×960), the error in 2D Keypoint Detection is required to not exceed 10 pixels. Considering the radius of the drill tip ($r_d = 0.5$ mm) and the manually set offset ($\Delta d = 0.5$ mm) in (15), the errors of Landmark Calibration is required to not exceed 1 mm.

3) *Result and discussion:* As shown in Fig. 7, we randomly generated 20 coordinates as validation setpoints within the reconstruction space of MSCS, and observed an RMSE of 3.18 pixels in 2D Keypoint Detection and 0.77 mm in Landmark Calibration, which meet our accuracy requirement, indicating a high overall detection and calibration precision. However, as shown in Fig. 7-(b), 4 points exceeded the error threshold for Landmark Calibration, likely due to MSCS reconstruction limitations. While acceptable in Experiment 1, they may cause milling failures in the subsequent Experiment 2. To mitigate this, future work will focus on further enhancing 3D reconstruction accuracy with higher-resolution cameras and more robust models.

D. Experiment 2: Validation of 3D Surface Fitting

As described in Section IV-B, the accuracy of 3D Surface Fitting is affected by the accuracy of Trajectory Center Localization and 3D-fitted Initial Trajectory Generation. As the performance of 3D-fitted Initial Trajectory Generation is based on the reconstruction of the target surface which has been evaluated in [10], and the transformation obtained via Landmark Calibration which has been evaluated in Section V-C, in Experiment 2, we focus on the evaluation of Trajectory Center Localization.

1) *Training of CNN model:* To prepare learning data, a dataset consisting of 523 images that satisfy the requirement that the mouse skulls in the images remain unmilled were captured from videos of the same 10 euthanized mice mentioned in Section V-C, as well as 82 images from a publicly available dataset created by [16]. The creation of ground truths and data augmentation are the same as Section V-C, resulting in a total of 8,774 images, with 7,019 for training, 877 for validation, and 878 for testing (an example is shown

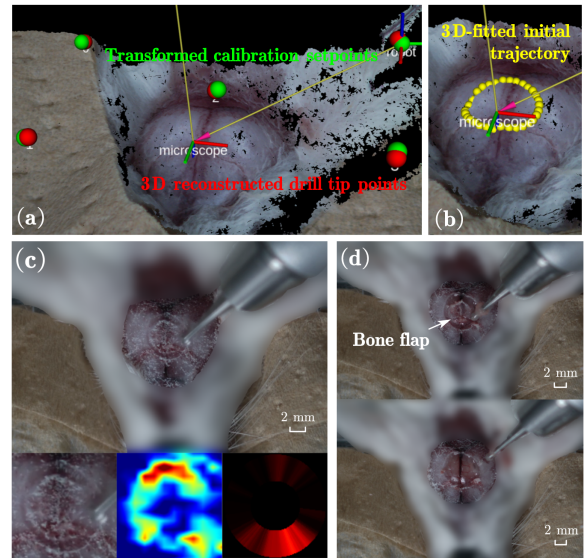


Fig. 8. The automation flow of an experimental case. (a) The result of Automatic Calibration (Section IV-A). (b) The result of 3D Surface Fitting (Section IV-B). (c) The input and output of the Completion Level Recognition (Section III-A). (d) The result after the milling process was completed and after the bone flap was manually removed.

in Fig. 6-(b)). The training condition and parameters are also as same as Section V-C.

2) *Metrics:* Considering that the trajectory center is calculated by linearly weighting the detected bregma and lambda, with the detection errors of these two points considered independent, the error of Trajectory Center Localization can also be calculated by linearly weighting the detection RMSE of bregma and lambda. Same as Section V-C, we require the error not to exceed 10 pixels.

3) *Result and discussion:* In the test dataset, we observed an RMSE of 1.19 pixels for bregma detection and 1.73 pixels for lambda detection. The RMSE for lambda was higher than that for bregma, possibly because bregma is more distinguishable than lambda, even for humans. By applying linear weighting to integrate the information from both, the RMSE of the trajectory center was 1.37 pixels, meeting the accuracy requirement.

E. Experiment 3: Validation of the autonomous robotic bone micro-milling system

Using the autonomous robotic bone micro-milling system shown in Fig. 1, with its hardware setup described in Section II, cranial window creation experiments were conducted on euthanized mice to validate the feasibility of the proposed method.

1) *Animal model:* All experiments were performed on euthanized mice euthanized with carbon dioxide, approved by the Animal Care and Use Committee, Graduate School of Medicine, The University of Tokyo (Approval No.: A2023M042-04). The experiments were conducted in compliance with Fundamental Guidelines for Proper Conduct of Animal Experiment and Related Activities in Academic Research Institutions (2006), MEXT Japan, and Guidelines

for Proper Conduct of Animal Experiments (2006) Science Council of Japan. 7 female NOD.CB17-Prkdc^{scid}/J mice, aged 6 to 8 weeks and weighing 20-25 g, are used in the experiments.

2) *Metrics*: Milling success and time are used to evaluate the performance. It should be noted that milling success is defined as the bone flap (see Fig. 8-(d)) within the milling trajectory being removable manually with tweezers after the milling is completed, without damaging the membrane beneath the skull [8].

3) *Result and discussion*: 7 experiments were conducted, and 6 were successful, resulting in a success ratio of 85.7%. The average required time for successful milling was 2.1 ± 1.8 minutes. Compared with the 80% of success ratio and the 16.8 ± 2.5 minutes of milling time using the previous system [8] evaluated on eggshell model, the feasibility and efficiency of the improved autonomous robotic bone micro-milling scheme were initially proved on euthanized mice. An example of the entire flow of a successful milling case is shown in Fig. 8. The improvement in success ratio and the reduction in milling time aligned with our expectations, as the introduction of MSCS enhanced the system's perceptual capability for uneven surfaces, avoiding the long milling time and potential failures caused by the complete reliance on real-time feedback in the previous system.

Furthermore, compared with the results of teleoperated robotic cranial window creation mentioned in Section V-C (13.7 ± 6.6 minutes, 3 skilled and 4 novice human operators, 10 euthanized mice) and manual cranial window creation [6] (8.0 ± 2.1 minutes, 2 skilled human operators, 6 anesthetized live mice), the system is demonstrated with excellent speed, repeatability, and consistency.

The error in Completion Level Recognition is considered the main cause of the failure case, indicating that the recognition accuracy of the CNN relying solely on RGB images limits the upper bound of the success ratio. Future work will require improving the recognition accuracy of the CNN or adding additional sensors to assist with image processing.

VI. DISCUSSION AND CONCLUSIONS

In this paper, we propose an automatic calibration and 3D surface fitting method and integrate it with an autonomous robotic bone micro-milling system, enabling it to rapidly, real-time, and accurately perceive and adapt to the uneven surface and non-uniform thickness of bone tissue without human assistance. In the experiments, we validated the system's excellent performance and efficiency by successfully performing autonomous cranial window creation on euthanized mice, achieving faster, more accurate and more stable results compared to skilled human operators.

Future works include further improving the performance of the system and applying the system on anesthetized live mice. In addition, considering the similar challenges of target surface and thickness uncertainties in many surgeries, such as endoscopic endonasal surgery and neural surgery, we also hope to apply our autonomous robotic bone micro-drilling system to other medical fields.

ACKNOWLEDGMENT

We would like to express our special gratitude to Dr. Saúl Alexis Heredia Pérez, Dr. Murilo Marques Marinho and the surgeons in Institute of Science Tokyo for their precious advice and kind help.

REFERENCES

- [1] Y. Liu, B. Chen, and A. Li, "Fracture mechanical properties and fractal analysis of fracture surfaces of cortical bone," *Journal of Biomaterials and Tissue Engineering*, vol. 9, no. 4, pp. 443–449, 2019.
- [2] P. Shang, H. Zhang, X. Liu, Z. Yang, B. Liu, and T. Liu, "Cutting-force modeling study on vibration-assisted micro-milling of bone materials," *Micromachines*, vol. 14, no. 7, p. 1422, 2023.
- [3] T. Takebe and J. M. Wells, "Organoids by design," *Science*, vol. 364, no. 6444, pp. 956–959, Jun. 2019, publisher: American Association for the Advancement of Science.
- [4] N. Pak, J. H. Siegle, J. P. Kinney, D. J. Denman, T. J. Blanche, and E. S. Boyden, "Closed-loop, ultraprecise, automated craniotomies," *Journal of Neurophysiology*, vol. 113, no. 10, pp. 3943–3953, Jun. 2015.
- [5] L. Ghanbari, M. L. Rynes, J. Hu, D. S. Schulman, G. W. Johnson, M. Laroque, G. M. Shull, and S. B. Kodandaramaiah, "Craniobot: A computer numerical controlled robot for cranial microsurgeries," *Scientific reports*, vol. 9, no. 1, p. 1023, 2019, publisher: Nature Publishing Group UK London.
- [6] Z. S. Navabi, R. Peters, B. Gulner, A. Cherkkil, E. Ko, F. Dadashi, J. O'Brien, M. Feldkamp, and S. B. Kodandaramaiah, "Computer vision guided rapid and precise automated cranial microsurgeries in rodents," *bioRxiv*, pp. 2024–09, 2024.
- [7] D. C. Jeong, P. S. Tsai, and D. Kleinfeld, "All-optical osteotomy to create windows for transcranial imaging in mice," *Optics Express*, vol. 21, no. 20, pp. 23 160–23 168, 2013.
- [8] E. Zhao, M. M. Marinho, and K. Harada, "Autonomous Robotic Drilling System for Mice Cranial Window Creation: An Evaluation with an Egg Model," in *2023 IEEE/RSJ International Conference on Intelligent Robots and Systems (IROS)*, Oct. 2023, pp. 4592–4599, arXiv:2303.12265 [cs].
- [9] M. M. Marinho, J. J. Quiroz-Omaña, and K. Harada, "A Multiarm Robotic Platform for Scientific Exploration: Its Design, Digital Twins, and Validation," *IEEE Robotics & Automation Magazine*, 2024, publisher: IEEE.
- [10] X. Lin, S. A. Heredia Pérez, and K. Harada, "A cranial-feature-based registration scheme for robotic micromanipulation using a microscopic stereo camera system," *Advanced Robotics*, vol. 38, no. 24, pp. 1730–1742, Dec. 2024, publisher: Taylor & Francis. eprint: <https://doi.org/10.1080/01691864.2024.2415092>.
- [11] C. Kruger, "Constrained cubic spline interpolation," *Chemical Engineering Applications*, vol. 1, no. 1, 2003.
- [12] S. Garrido-Jurado, R. Muñoz-Salinas, F. J. Madrid-Cuevas, and M. J. Marín-Jiménez, "Automatic generation and detection of highly reliable fiducial markers under occlusion," *Pattern Recognition*, vol. 47, no. 6, pp. 2280–2292, 2014.
- [13] Z. Zhang, "A flexible new technique for camera calibration," *IEEE Transactions on pattern analysis and machine intelligence*, vol. 22, no. 11, pp. 1330–1334, 2000.
- [14] M. Manafifard, "A review on camera calibration in soccer videos," *Multimedia Tools and Applications*, vol. 83, no. 6, pp. 18 427–18 458, 2024.
- [15] O. Ronneberger, P. Fischer, and T. Brox, "U-net: Convolutional networks for biomedical image segmentation," in *Medical image computing and computer-assisted intervention—MICCAI 2015: 18th international conference, Munich, Germany, October 5–9, 2015, proceedings, part III 18*. Springer, 2015, pp. 234–241.
- [16] P. Zhou, Z. Liu, H. Wu, Y. Wang, Y. Lei, and S. Abbaszadeh, "Automatically detecting bregma and lambda points in rodent skull anatomy images," *PLoS one*, vol. 15, no. 12, p. e0244378, 2020.
- [17] B. V. Adorno and M. Marques Marinho, "Dq robotics: A library for robot modeling and control," *IEEE Robotics & Automation Magazine*, vol. 28, no. 3, pp. 102–116, 2021.